



Research article

Local strain quantification of a porous carbon fiber network material

R.N. Quammen, P.F. Rottmann *

University of Kentucky, Department of Materials Science and Engineering, 177 F. Paul Anderson Tower, Lexington, KY, 40506, USA

ARTICLE INFO

Keywords:

Compressive mechanical properties
Deformation behavior
Digital image correlation (DIC)
Fibrous network material
Carbon fiber

ABSTRACT

While porous materials' wide range of attractive functional properties have led to their development for a variety of applications, their intrinsically stochastic microstructures prevent straightforward approaches to predicting their mechanical behavior. This is attributed to the mechanisms that govern the macroscale behavior of these materials operating on multiple microstructure-specific length scales spanning several orders of magnitude. The goal of this work was to experimentally observe these operative deformation mechanisms to better improve the development of mechanism-informed models that more accurately predict the behavior of these materials. In this study compression tests were conducted on a porous carbon fiber network material. The resulting macroscale mechanical properties and mesoscale deformation behavior were tied together through digital image correlation (DIC) strain mapping. It was shown that deformation accumulation occurred via both reversible (fiber bending and sliding) and irreversible (fiber and junction failure) ways. The presence of irreversible deformation is indicated by strain being retained after unloading, with values of up to 0.426 locally and 0.248 globally. Local and macroscopic recovery of up to 0.306 and 0.207 strain respectively showcase the operation of reversible deformation. Furthermore, the calculation of energy loss coefficients increasing from 0.016 to 0.371 illustrates that the deformation occurs via dissipative mechanisms.

1. Introduction

Low-density porous materials are used in a wide variety of applications due to their vast range of mechanical and functional properties not accessible through fully dense materials. Catalysis [1], energy storage [2], medicine [3], electronics [4], and aerospace [5] are just a few of the industries in which these materials are being used. Nanoporous metals and metal foams [6], polymer foams [7], and porous fiber networks [8] are some common types of low-density porous materials, with each exhibiting dissimilar mechanical behaviors under load.

Recently, the interest in modeling the mechanical behavior of porous fiber network materials has increased. Fiber breakage and fiber bending were both identified as mesoscale deformation mechanisms in bonded inorganic fiber networks by Liu et al. [9]. The significant effect of preferred fiber orientation on the mechanical behavior of SiO₂ ceramic fibers was demonstrated by Shi et al. in compression testing, shear testing, and finite element modeling [10]. A reinvestigation of the computational models relating uniaxial compressive stress to density for non-crosslinked fiber networks was completed by Picu and Negi [11]. These models are of power law form with the scaling of stress, S , being $S \sim (\varphi^n - \varphi_0^n)$, with φ and φ_0 being the strain-dependent relative density and the initial

* Corresponding author.

E-mail address: paul.rottman@uky.edu (P.F. Rottmann).

relative density respectively. In this work, they confirmed an exponent of $n = 3$ proposed by Van Wyk [12] for low densities/levels of compression; however, an exponent of $n = 2$ was observed to appear at higher densities/levels of compression. For random networks with high degrees of preferential alignment a value of $n = 5$ has been observed by Toll and Mason [13] but was not verified in the Picu and Negi study.

These efforts have been successful in improving the prediction of ‘bulk’ yield strength and elastic modulus as well as beginning to explain interactions at the individual ligament/fiber scale. However, the propagation of the ligament/fiber level interactions to the mesoscale and the ensuing effects on macroscale mechanical properties are not well understood. The multi-scale structure-properties relationships associated with this are complex and require an understanding of the varied deformation mechanisms present and the effect of microstructural stochasticity.

Probing the requisite size scales in a way that the mechanical properties and deformation behaviors can be observed directly is challenging due primarily to their small size and that they operate in difficult-to-view, subsurface regions. One potential path forward is using digital image correlation (DIC). With DIC, deformation and strain maps are created by comparing successive images of the sample during testing [14–16]. This provides high-resolution 2D strain data from the deforming surface which, when coupled with stress data collected in parallel, provides a direct window into the initiation and accumulation of deformation. This technique has proven to be extremely successful in elucidating the details of dislocation-mediated plasticity in metals not accessible using conventional mechanical testing [17–19]. It has also been used to observe the non-linear deformation of a biological fibrous network called mycelium [20].

In the current work, a low-density, porous fiber material called FiberForm was utilized to investigate the tie between its macroscale mechanical properties and the mesoscale deformation and strain localization behavior. This material is the substrate in Phenolic-Impregnated Carbon Ablator (PICA), which is utilized as a heat shield for thermal protection systems (TPS). The macroscale and microscale structure of FiberForm are shown in Fig. 1 and are similar to that of other comparable materials in literature [21–23]. The mechanical properties have been investigated to some capacity both computationally [24–26] and experimentally [21,22,27]. Variations in macroscale stress-strain behavior based on loading orientation were observed by Parmenter et al., with these variations persisting even after impregnation with phenolic resin to create PICA [21]. FiberForm fracture at the fiber level via fiber pullout for notched samples in tension was observed by Agrawal et al. [27]. More recently, Zhang et al. [22] demonstrated the importance of factors such as fiber length, fiber orientation, and fiber density in the macroscale mechanical performance of FiberForm-like materials. Zhang et al. [28] additionally illustrated the fiber-level deformation mechanisms exhibited by FiberForm-like materials under cyclic compression. Work on a similar porous fibrous network material by Luo et al. showed layer-by-layer damage which was subsequently modeled using an equivalent stiffness method [26].

The operative microscale and local deformation mechanisms for fibrous network materials along with their impact on the resulting macroscale mechanical properties are still not well understood or modeled in current literature. To investigate the complex and poorly understood ties between size scales, compression tests with corresponding DIC were completed on FiberForm. Compression testing was used due to the widely applicable macroscale properties that could be obtained for comparison to published studies in the literature (e. g. elastic modulus and compressive strength). DIC imaging and analysis were used to determine the location, initiation, propagation, and growth of deformation and strain localization within the samples. This combination of results is useful to provide experimentally derived deformation mechanisms for use in the computational modeling of low-density, porous fiber materials. Additionally, this work showcases the promise of DIC as an avenue to investigate the mesoscale deformation mechanisms that govern the properties of low-density, porous materials as a whole.

2. Methods

2.1. Sample preparation

Rectangular specimens of approximately 15 mm long by 12 mm wide by 12 mm thick (exact measurements in [Supplementary](#)

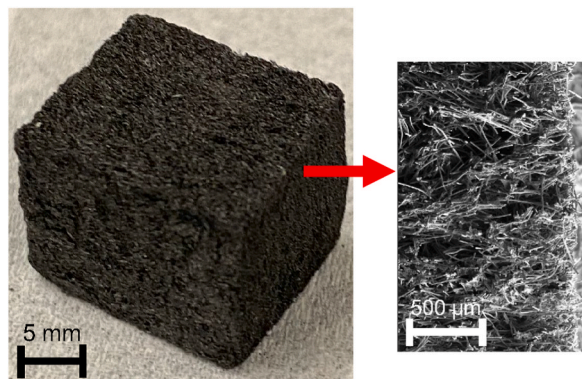


Fig. 1. Images showing the macroscale (left) and secondary electron SEM image (right) showing the microscale structure of FiberForm.

Material Table S1) were cut from large blocks of FiberForm. Test specimens were further shaped to ensure flat, parallel surfaces on all sides manually by razor and CNC milling. The provided FiberForm preform had a chopped fiber length of approximately 1 mm, fiber diameter of 11 μm , pyrolyzed carbon crosslinks, and targeted porosity of 90%. Samples were cut with the length axis both parallel (designated as the ‘out-of-plane’ or OOP samples) and perpendicular (designated as the ‘in-plane’ or IP samples) to the build direction of the FiberForm block, as shown in Supplementary Material Fig. S1. Due to the fabrication process, the general fiber orientation is perpendicular to the build direction. Both loading orientations were tested to obtain information regarding the transversely isotropic properties of this material. Calipers were used to measure each side to the hundredth of a millimeter and a maximum variability of 0.1 mm was allowed to ensure sample uniformity.

2.2. Compression testing

Compression testing was conducted utilizing a custom, in-lab, ex-situ micromechanical testing setup. The setup consisted of a PI L-239.50SD linear actuator with a minimum step size of 0.1 μm connected to a moving crosshead platen, a Futek LSB205 load cell with a maximum capacity of 100 lbs attached to a stationary crosshead to obtain load data, and an in-line linear air bearing to ensure alignment and accurate force reading by the load cell. The system was also equipped with a Balsa Ace acA2440 camera containing a Sony IMX250 CMOS sensor with 5 MP resolution and 75 fps frame rate for use in 2D DIC. Correlated Solutions Vic-Gauge software was used in conjunction with this camera to obtain images to track the displacement during all compression tests. The entire setup was secured to an optical table to minimize vibrational influence.

Compression tests were run using a custom Python script. Tests were displacement controlled, completed at a displacement rate of 1 mm/min (strain rate of approximately 0.001 s^{-1} - 0.0017 s^{-1}), and conducted both IP and OOP. The relationship between loading orientation and general fiber orientation observed during testing is illustrated in Fig. 2a and b for OOP and IP, respectively. All IP samples and OOP Samples 1–4 were tested to 4 mm displacement (approximately 26.7% compression) to provide information regarding the general deformation behavior exhibited by each loading orientation. OOP Sample 5 was tested to 10 mm displacement (approximately 66.7% compression) to investigate the ultimate failure of the out-of-plane specimens. Stress was calculated for all tests by dividing the load output from the load cell by the initial cross-sectional area (width times thickness) thus giving engineering stress. Strain measurements were provided via a virtual strain gauge in the Vic-Gauge software. The virtual strain gauge, however, provided only a 1D average strain measured by locations near the crossheads. To obtain a more accurate representation of strain across the entire sample, local strain values across the entire specimen surface were averaged instead, as described below in Section 2.3.

A single compression test with load-unload cycling was also completed in the OOP loading direction (called OOP Load-Unload). The test used the same test setup and image acquisition as the monotonic compression tests. A displacement rate of 1 mm/min (0.0017 s^{-1} strain rate) was used for both loading and unloading. Unloading was completed to a stress of $\sim 0.0025 \text{ MPa}$ to ensure as much recovery as possible could occur while also maintaining contact between the sample and crossheads. During this test, 3 load-unload cycles were completed at three separate displacements of 0.75 mm, 3 mm, and 5 mm (called $\bar{\epsilon}_1$, $\bar{\epsilon}_2$, and $\bar{\epsilon}_3$ from here on) with a final loading to a displacement of 6 mm. These four displacements correspond to macroscopic strains of 0.02, 0.23, 0.42, and 0.50 and were chosen to investigate sample recovery at low, moderate, and high strains. Quantification of the energy dissipation during load-unload cycling was completed through the use of the energy loss coefficient, which has been used in previous literature [28]. This coefficient was calculated by dividing the dissipated energy for a given cycle by the overall strain energy for a given cycle. Area under the loading portion of the cycle was used as the overall strain energy and area between the loading and unloading portions was used as the dissipated energy. The trapezoidal integration method was used for the calculation of the areas. The fraction of the sample experiencing strain localization was also calculated for this test by dividing the number of pixels with a strain of greater than 0.05 by the total number of pixels. A strain of 0.05 was determined to be a sufficient cutoff to be considered appreciable deformation through comparison of localization regions to regions not experiencing localization, as is illustrated in Section 3.2.

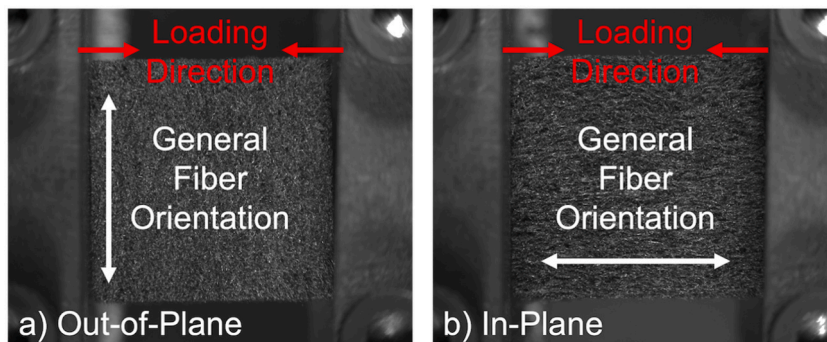


Fig. 2. Images showing loading direction and general fiber orientation for a) out-of-plane (OOP) and b) in-plane (IP) samples during compression testing.

2.3. Digital image correlation

Quantification of strain evolution across the entire sample surface over the duration of the test was achieved via DIC using images obtained at 500 ms intervals throughout the tests. 2-D strain color maps with minimum resolution of 10^{-6} strain were created for the top surface of each sample to identify the onset and propagation of strain localization and enable correlation between strain localization and macroscopic stress-strain behavior. Images were imported to Correlated Solutions Vic-2D software for final analysis. The as-cut FiberForm surfaces were used during testing and analysis as they provided sufficient contrast for DIC tracking from image to image; an example image showing the stochastic contrast of the as-cut sample surface is shown in [Supplementary Material Fig. S2](#). Data points were created over the entire top surface of each sample using the chosen subset size and step size. Subset size was the side length in pixels of the square region comprising each data point and the step size was the pixel distance between each data point. During the analyses, a step size of 5 pixels (approximately 0.04 mm) was chosen for all samples to optimize data retention and analysis speed. The subset sizes chosen ranged from 71 – 91 pixels (approximately 0.6 – 0.75 mm), with larger subset sizes being necessary for larger deformations. Incremental correlation (comparing each image to the previous image) was utilized to further optimize data retention. A confidence margin threshold of 0.05 pixels was used to minimize the number of incorrect matches appearing in the data set.

Local strain for each subset was calculated within the Vic-2D software utilizing continuum mechanics approaches [29,30]. Deformation is represented in terms of engineering strain, as this tensor provides the best comparison to values obtained throughout other experimental literature. The mean, minimum, and maximum of the local strain and in-plane rotation values for all subsets were exported for each image. The mean value was considered the average strain over the entire sample and was used in the creation of the stress-strain plots. Quantification of localized strain was completed by identification through visual inspection and then a polygon was manually created encompassing the area with the outer edge of the polygon correlating to approximately 1/4th of the largest compressive strain experienced by the sample throughout the duration of the test (this value varied from sample to sample).

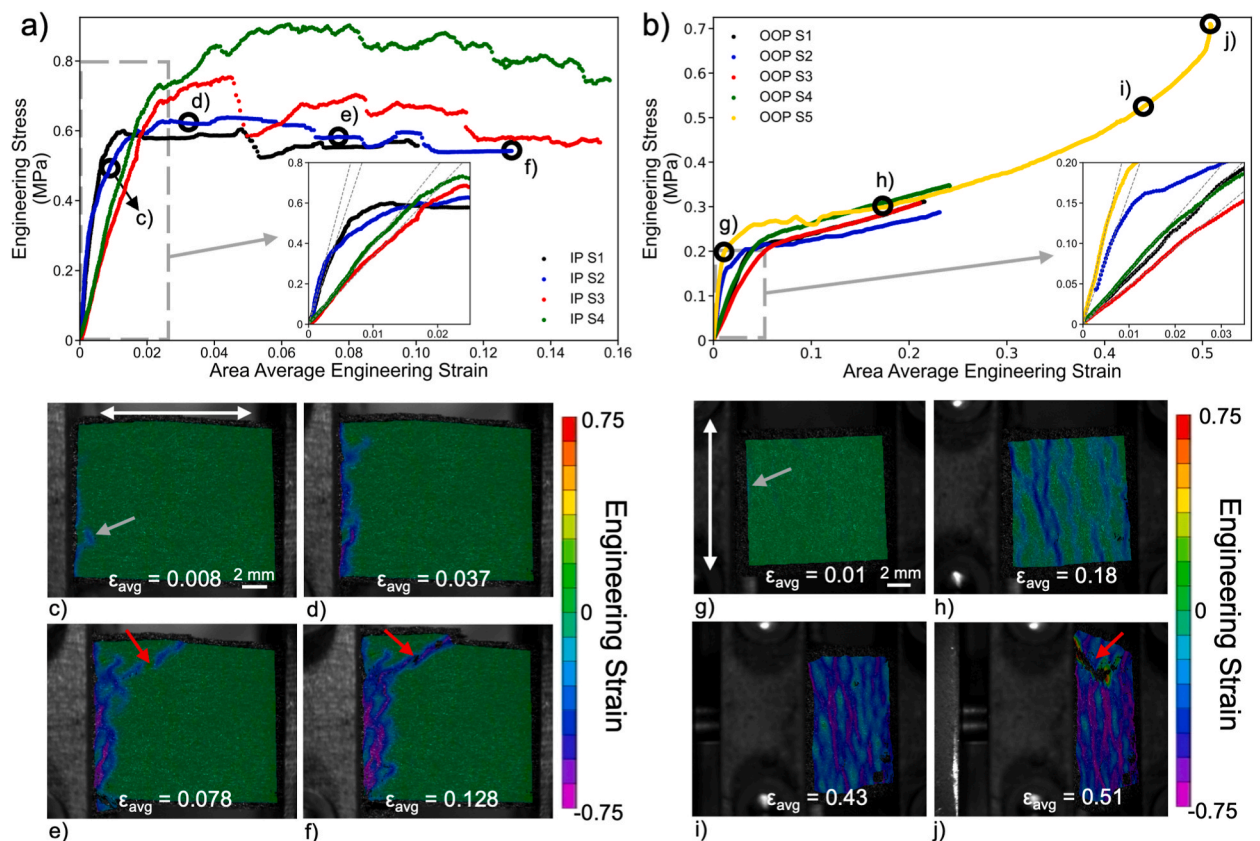


Fig. 3. Stress strain curves for a) in-plane loading and b) out-of-plane loading of compression samples. Black circles correspond to [Fig. 3c–f](#) and [3g–j](#) for in-plane and out-of-plane loading, respectively. Insets show regions utilized for obtaining effective elastic modulus for each sample with grey dashed line corresponding to slope of line equal to elastic modulus for each sample. DIC analysis images showing strain localization during in-plane compression are shown in [c\) – f\)](#) and during out-of-plane compression are shown in [g\) – j\)](#). White arrows in [c\)](#) and [g\)](#) indicate general fiber orientation while grey arrows indicate strain localization initiation. Red arrows in [e\)](#), [f\)](#), and [j\)](#) indicate where failure occurred within the samples.

3. Results

3.1. Determination of loading-orientation-dependent mechanical behavior

3.1.1. Macroscale mechanical properties

The deformation behavior of the porous carbon fiber network in both the out-of-plane and in-plane loading orientations was assessed utilizing compression testing. Monotonic compressive loading tests were completed to displacements of 4 mm and 10 mm as stated in Sections 2.2 and 2.3 and the stress-strain curves are displayed in Fig. 3. During the in-plane tests (shown in Fig. 3a), there is initially a sharp increase in stress while undergoing minimal strain. From this region the elastic modulus was determined and is indicated via the inset in Fig. 3a. The elastic moduli for the four tests conducted in this loading orientation are shown in Table 1. A 'yield' type event then occurs with compressive strain where deformation continues with little increase in stress for the remainder of the test. The maximum compressive stress before failure is also listed in Table 1 for the in-plane loaded samples.

The appearance of the elastic and damage accumulation behaviors exhibited for the out-of-plane loaded samples is distinct from that observed in the in-plane loading orientation, as demonstrated in Fig. 3b. In the elastic region, a much lower stress increase is experienced in conjunction with an appreciable change in strain indicating that the out-of-plane samples have a lower resistance to elastic compression. This is shown by the elastic moduli values displayed in Table 2. Once damage accumulation initiates, increasing stress is required to impose further deformation resulting in a monotonic stress increase for out-of-plane loading instead of the stress plateau observed for in-plane loading. The maximum compressive stress before failure was only obtained for the Sample 5, as listed in Table 2, as that is the only out-of-plane sample that was tested to failure. Maximum compressive stresses from all other out-of-plane samples are only a function of when the test was stopped during the damage accumulation portion of the stress-strain curve.

3.1.2. Mesoscale deformation behavior

DIC analysis of the onset and evolution of strain across each sample was also used to investigate the distinct deformation behaviors exhibited by both the in-plane and out-of-plane loading orientations. Fig. 3c–f displays four DIC images correlating to the black circles on the IP S2 stress-strain curve in Fig. 3a. Videos of the DIC analysis and stress-strain curve progression for all samples are provided in the Supplementary Material Figs. S3–S11. From Fig. 3c–f there is an increase in the amount of strain being imposed on the sample as indicated by the increase of blue/purple regions in the images. The appearance of specific bands of higher compressive strain instead of uniform change across the entire sample illustrates strain localization is occurring. For this sample, strain is localized only near the left crosshead. As the deformation of the material proceeds, strain localizes in the area contacting the left crosshead and propagates at an angle inclined to the average fiber direction. Furthermore, the strain experienced by regions on the right side of the sample is essentially zero indicating that the deformation accumulation is only occurring in a small fraction of the sample on the left crosshead edge. This behavior of strong strain localization persisting near a crosshead edge of the sample and only moving inward after significant compression occurs is consistent for the in-plane samples. All in-plane samples also exhibited global failure on planes inclined with respect to the compression axis, as is signified by the red arrows in Fig. 3e and f. This behavior is analogous to catastrophic shearing in fully dense materials [31,32].

The strain evolution within an out-of-plane loaded sample is shown in Fig. 3g–j, which displays four DIC images correlating to the black circles on the OOP S5 stress-strain curve in Fig. 3b. Similar to the in-plane loading orientation, an increase in the strain experienced by the sample is evident due to the appearance of strain localization regions. Furthermore, in Fig. 3g, these strain localization regions initiate near the crosshead edge, like those seen in Fig. 3c. The catastrophic shearing mode of failure is also consistent between the two loading orientations (Fig. 3f and j) but occurred at a much higher strain for out-of-plane loading. In contrast to the in-plane samples, after initiation of deformation accumulation, the localization quickly propagates toward the center of the sample (Fig. 3h). Additionally, the strain localization bands generally span the entire width of the sample parallel to the general fiber orientation, as shown in Fig. 3h–j. These bands are also distributed throughout the length of the sample and result in the regions that do not accumulate damage being in the minority by the end of the test, as Fig. 3i and j displays. These behaviors were consistent for this loading orientation.

3.2. Mesoscale strain localization, initiation, and evolution

In addition to global deformation behavior and the location of strain localization, DIC also allows for analysis of the time-dependent accumulation of strain at regions of interest. Investigating this gives specific information about the initiation, propagation, and growth of strain localization bands across a sample that can then be tied back to characteristics in the macroscale mechanical properties. To perform this analysis, plots showing the evolution of strain in eventual localization bands throughout the duration of a test for OOP S2 were created as shown in Fig. 4. In this figure the time over which the test occurs is on the x-axis and the change in strain is on the y-

Table 1
In-plane compression properties.

Sample	IP S1	IP S2	IP S3	IP S4
Effective Elastic Modulus (MPa)	91.82	128.31	32.94	35.10
Yield Stress (MPa)	0.449	0.323	0.656	0.725
Maximum Compressive Stress Before Failure (MPa)	0.604	0.639	0.754	0.905

Table 2
Out-of-plane compression properties.

Sample	OOP S1	OOP S2	OOP S3	OOP S4	OOP S5
Effective Elastic Modulus (MPa)	5.27	16.31	4.05	5.45	20.91
Yield Stress (MPa)	0.204	0.138	0.191	0.193	0.196
Maximum Compressive Stress Before Failure (MPa)	–	–	–	–	0.714

axis. Each ‘Region’ curve in this plot corresponds to a specific strain localization band in the accompanying DIC image outlined in the color coordinating with the color of the curve in the plot. Curves showing the change in the global average strain (dashed red) as well as of a region that did not experience strong strain localization (‘Background’) are also provided. The ‘Background’ curve was included to illustrate the amount of strain accommodated by the regions that do not accumulate damage.

When considering the ‘Average’ and ‘Background’ curves they have distinctly different behavior than the ‘Region’ curves. The ‘Average’ curve has a consistent linear increase in strain over the course of the test (strain rate of 0.0012 s^{-1}), which is experienced by all samples no matter loading orientation and is expected given the continual compressive displacement applied to the samples. The ‘Background’ curve can be seen to barely deviate from 0 until the end of the test. Having such a low value for the ‘Background’ compressive strain indicates that essentially all the deformation undergone by the sample is restricted to the strain localization bands.

In the plot in Fig. 4, ‘Region 1’ is the area where damage accumulation begins as evidenced by it being the first area to experience appreciable compressive strain at a strain rate of 0.0065 s^{-1} . As the global compressive displacement increases, the local compressive strain is fully accommodated in this area. Eventually, ‘Region 1’ reaches a local compressive strain of approximately 0.15 and stops accommodating strain completely. The continued global compressive displacement is then instead accommodated by ‘Region 2’ at a strain rate of 0.0042 s^{-1} thus showcasing the propagation of sequential damage accumulation in this material. Multiple areas locally deforming simultaneously is also a form of sequential damage accumulation observed in Fig. 4. This is illustrated at the 115-s mark when the global compressive displacement reaches a point where it can no longer be only accommodated by ‘Region 2’ and thus ‘Region 3’ begins to locally deform as well at a strain rate of 0.0079 s^{-1} . The accommodation of global compressive displacement in all three regions can be seen after the 125-s mark. Discussion on the reasoning behind the sequential damage accumulation is in Sections 4.1 and 4.2.1.

3.3. Recovery and hysteresis during load-unload cycling

To systematically assess the elastic recovery and energy dissipation as a function of global strain a single sample was tested using a load-unload cycling experiment. Fig. 5 displays two plots with the one in Fig. 5a showing the stress-strain curve for OOP Load-Unload on the left y-axis and the fraction of data points in the sample experiencing strain localization on the right y-axis. Fig. 5b shows the change in compressive strain from the beginning (marker) to the end (horizontal line) of unloading of each cycle for the full sample (red), first strain localization region (blue), and final strain localization region (grey) at each strain level on the left y-axis. The right y-axis displays the energy loss coefficient calculated for each cycle at all three strain levels. DIC images are displayed in Fig. 5c–f corresponding to the circles on the green dashed line in Fig. 5a.

Comparing the stress-strain curve in Fig. 5a to the monotonic tests in Fig. 3b, outside of the cycling, there is a similar monotonic increase in stress with increasing strain. Additionally, the elastic modulus (16.35 MPa) and yield stress (0.236 MPa) are in line with that obtained for the other OOP samples in this study. These similarities to the monotonic samples also translated to the strain localization and propagation behavior observed via DIC, which can be seen in the video in Supplementary Material Figure S12 and Fig. 5c–f. As is shown in these figures, layer-by-layer deformation occurs and ends up propagating throughout the sample with the

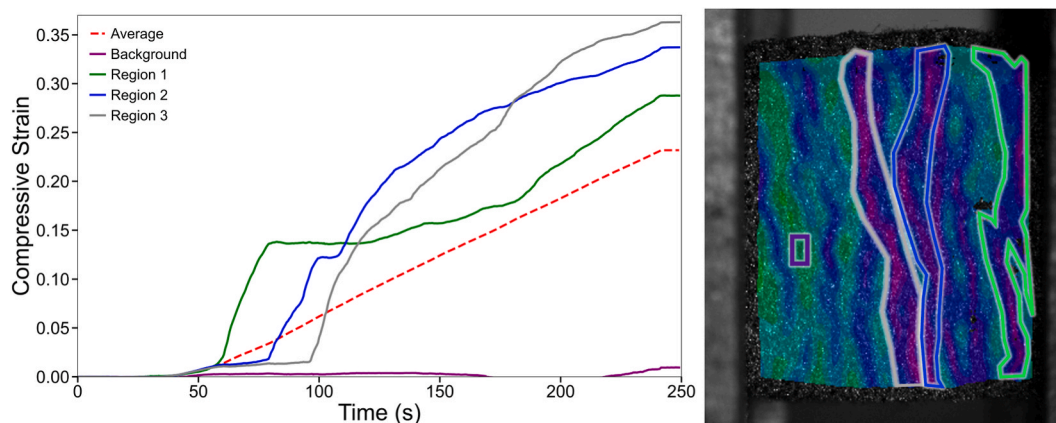


Fig. 4. Plot showing strain localization behavior caused by sequential damage accumulation during compression. Outlined areas in right DIC image correspond to the curves on the left plot. DIC image is from end of a compression test in the out-of-plane orientation.

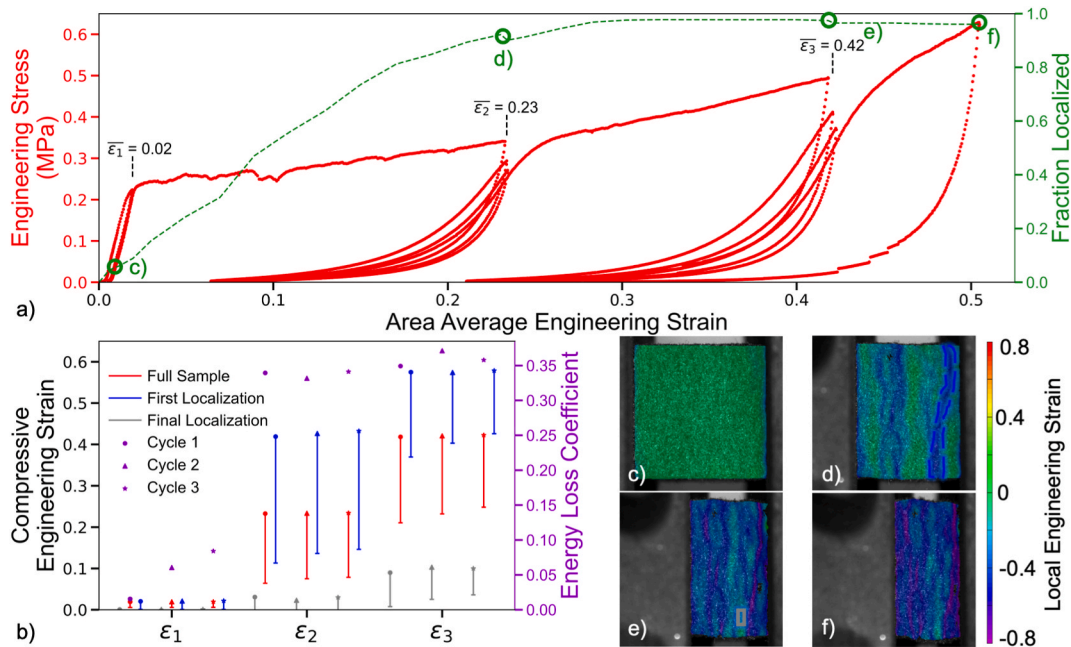


Fig. 5. a) Plot showing OOP Load-Unload stress-strain curve (red) and fraction of the sample that is experiencing strain localization (green). Labels on dashed green curve correspond to DIC images in c) – f). Annotation added to stress-strain plot to identify strain range for cycling at each different strain level. b) Plot showing relationship between maximum compressive strain (marker) and strain at the end of unloading (horizontal line) for full sample, first localization region (identified by blue dashed region in d)), and final localization region (identified by grey dashed region in e)) at each strain level for all three cycles. Energy loss coefficient (purple) is also plotted for each cycle at all three strain levels.

majority (>95%) of the sample experiencing strain localization at the end of the test.

Investigating the load-unload cycling specifically, hysteresis was observed between the unload and reload curves for each sample. This is illustrated by the gap observed between the unload and reload curves during cycling in Fig. 5a and is indicative of energy dissipation occurring. As shown in Fig. 5b, the energy loss coefficient increases from approximately 0.05 at $\bar{\epsilon}_1$ to approximately 0.35 at $\bar{\epsilon}_3$. Another key result from this test was that as the cycle number increased, the retained strain at the end of unloading increased. This occurred at all strain levels but is most apparent for $\bar{\epsilon}_3$ where retained strain increased from 0.211 to 0.248 for the entire sample. This increase in retained strain also correlates with a decrease in compressive stress at unloading strain for increasing cycle number. Again, for $\bar{\epsilon}_3$, the maximum compressive stress before the first unload is 0.494 MPa which decreases to 0.327 MPa on the last loading cycle. Even though some strain is retained there is still recovery that occurs from the maximum compressive strain achieved before unloading to the end of unloading as illustrated in Fig. 5a and b. The largest recovery achieved for the full sample was during the first cycle of $\bar{\epsilon}_3$ with 0.207 strain recovered thus showcasing that the amount of recovery increases with increasing strain level. However, within a strain level the amount of recovery decreases with increasing cycle as shown by the third cycle of $\bar{\epsilon}_3$ only exhibiting a recovered strain of 0.175. This recovery is indicative of reversible deformation operating while the retained strain is indicative of irreversible deformation. The specific interpretations and implications of these results are discussed further in Section 4.

4. Discussion

As observed in Sections 3.1.2 and 3.2, deformation accumulation propagates heterogeneously through fibrous network materials such as FiberForm. This non-uniform deformation behavior takes different forms depending on the relationship between the loading axis and the general fiber orientation. For this study, in the case of out-of-plane loading damage accumulation initiates at one of the crosshead platens and then heterogeneously propagates throughout the material. This observed behavior is similar to that in 3D random fibrous network materials in both experiment and simulation [33,34]. This layer-by-layer deformation has been attributed to both fully reversible [28] and fully irreversible [25,26] deformation methods; however, according to this study both can appear to be active. With that in mind, discussion of where current interpretations and models are valid as well as nuances that need to be added are described in Sections 4.1 and 4.2.

4.1. Monotonic stress increase via increasing density

One of the key macroscale mechanical features of the OOP loaded samples was the monotonic stress increase that continued until failure. In work by Islam and Picu, it was shown that the dynamic formation of interfiber contacts during compression predominately dictates the macroscale stress-strain response observed for fibrous network materials [34]. From this work, a modified version of Toll's

analytical model relating interfiber contact density to compressive strain and fiber orientation was created with interfiber contact density increasing in a parabolic fashion with increasing volume fraction under compression. This increase in turn creates the observed monotonic stress increase due to new interfiber contacts increasing the resistance to continued deformation. Applying this model at the local level gives rise to a relatively straightforward explanation for the observed strain localization propagation behavior from Section 3.2. As a local region compresses the interfiber contact density and thus the deformation resistance in this region will increase. Eventually, this region will no longer have the lowest deformation resistance, and thus deformation will move to a different region where continued deformation accommodation is easier. At higher macroscale strains multiple regions can have similar deformation resistances thus resulting in accommodation in multiple regions at the same time, as was observed in Fig. 4 after the 125-s mark.

As the interfiber contact density increases there is a corresponding increase in the relative density of the fibrous network material. This relative density increase has been related to the monotonic stress increase in previous studies [11]. Fig. 6 shows a log-log plot of stress as a function of φ/φ_0 for each out-of-plane loaded sample in the post-elastic regime. For each of these samples a value of $n = 1.5 - 2$ was determined. As shown by Picu and Negi non-crosslinked fibrous networks exhibit a transition from $n = 3$, the value for van Wyk's expression [12], to $n = 2$ as the internal loading structure is created [11]. Since the internal loading structure is inherent to the FiberForm microstructure due to the crosslinks, no such transition should be expected and thus a value of $n \approx 2$ arises. While some preferential alignment is imparted during fabrication it is not to the severity required to result in a value of $n = 5$ that would be expected given Toll's model [13,35]. Previous studies noted a difference in n for non-crosslinked materials after loading and unloading a sample multiple times referred to as pre-conditioning [36]; however, for OOP Load-Unload exponents of $n = 1.56$ and $n = 1.52$ were calculated after cycling at ε_1 and ε_2 respectively suggesting the effect of pre-conditioning is lessened in materials with pre-existing cross-links.

As stated in Section 3.1, the monotonic stress increase behavior exhibited by OOP loading is not shared by IP loading due to the formation of new interfiber contacts being limited in this orientation. This limitation stems from loading along the fiber axis resulting in the fiber movement and sliding necessary for the formation of new interfiber contacts to be restricted. Instead, the load is transferred directly through the fibers and junctions resulting in potential junction failure and fiber buckling, as has been assumed in previous literature [22,26]. The lack of formation of new fiber contacts combined with these failure avenues results in the observed stress plateau behavior and severe strain localization described in Section 3.1 for IP loading.

4.2. Combined recoverable and irrecoverable deformation behavior

4.2.1. Recovery and retained strain

In addition to the monotonic stress increase the large recovery observed during the testing of OOP Load-Unload is another key result from this work. This large recovery has also been previously observed by Zhang et al. [28] where it was posited that there was full recovery up to 40% strain. In contrast, though, Luo et al. [26] stated that the layer-by-layer deformation of these types of fibrous network materials occurred solely due to permanent damage in the regions of localization. The results from this study as argued below, however, indicate that the actual deformation behavior lies between these two interpretations, especially at moderate to high strains.

In Fig. 5b, it is evident that recovery is occurring at both the local (blue and grey) and macroscale (red) as illustrated by the decrease in compressive strain for both size scales throughout the unloading cycles. During unloading at a strain of 0.02 recovery is essentially complete at all length scales, in line with the observations of Zhang et al. [28]. This is further confirmed by the quantification of the maximum compressive strains and retained strains (in parentheses) listed in Table 3 which showcases that the strains drop well below the 0.05 strain cutoff chosen for indicating localization upon unloading. However, upon cycling at 0.23 and 0.42 both the full sample and first strain localization region retain appreciable strain (approximately 0.07 and approximately 0.130, respectively) thus

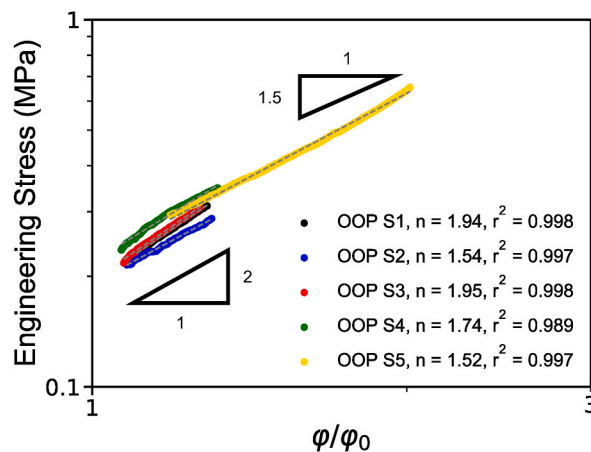


Fig. 6. Plot showing stress as a function of relative density. The axes are log-log and the horizontal axis is normalized by the initial relative density of the sample. The slope of each line as well as the r^2 of the power law fit are listed next to the sample. Inset slope triangles of 1.5 and 2 are added to visually compare the slope of each sample line.

Table 3
Maximum compressive strain and retained strain after unloading in parentheses.

	$\bar{\epsilon}_1$			$\bar{\epsilon}_2$			$\bar{\epsilon}_3$		
	Full Sample	First Localized	Final Localized	Full Sample	First Localized	Final Localized	Full Sample	First Localized	Final Localized
Cycle 1	0.019 (0.005)	0.020 (0.001)	0.001 (0.001)	0.233 (0.064)	0.419 (0.113)	0.031 (0.000)	0.418 (0.211)	0.575 (0.369)	0.090 (0.008)
Cycle 2	0.019 (0.006)	0.021 (0.001)	0.001 (0.001)	0.234 (0.075)	0.427 (0.136)	0.023 (0.000)	0.421 (0.232)	0.574 (0.403)	0.103 (0.025)
Cycle 3	0.019 (0.006)	0.022 (0.001)	0.001 (0.001)	0.234 (0.079)	0.432 (0.146)	0.030 (0.000)	0.423 (0.248)	0.579 (0.426)	0.100 (0.036)

indicating that some form of permanent deformation is occurring. This permanent deformation could take the form of junction failure, as was the assumed failure mechanism by Schill et al. [25], or fiber failure, as was used by Luo et al. [26] and can be classed as irreversible. As stated in Section 3.3, the amount of retained strain increases as a function of cycle within a strain level. This result implies that permanent deformation is not exhausted on initial loading to a specific strain. Due to the heterogeneous microstructure of the material, there are a variety of load-bearing pathways through the material. The distribution of load across these pathways changes as new contacts are formed and as the junctions and fibers fail. Therefore, when local failure occurs while loading to a specified strain, subsequent reloading to the same strain will result in different load profiles along the load-bearing pathways and thus further local failure and manifests in these results as increased retained strain with increase in cycle. Further evidence of this is shown by the decreasing macroscale stress with increasing cycle. Large amounts of recovery are still occurring at these strain levels though, which signifies that deformation is occurring via a combination of reversible and irreversible methods at moderate and high strains.

Further information regarding the deformation behavior of these types of materials can be determined through comparing the amount of recovery observed on both the local and macro scale. In Fig. 5b it is illustrated that at $\bar{\epsilon}_2$ the first localization region exhibits much larger recovery (0.294 average) compared to the full sample at the same strain level (0.161 average) and itself at ϵ_3 (0.177 average). From Fig. 5a the fraction of the sample exhibiting localization at $\bar{\epsilon}_2$ is high (>0.90), but Fig. 5d shows that there are only three regions displaying large amounts of strain localization (strain >0.40), with the first strain localization region having the most strain. Since only three areas are experiencing large amounts of localization and there is still available area in the sample not experiencing any localization it can be assumed that most of the deformation up to a strain of 0.23 is due to reversible methods (fiber sliding or rigid fiber motion/reorientation) resulting in new interfiber contacts, as was suggested by Islam and Picu [34]. Therefore, upon unloading at 0.23 strain, the first strain localization region will have the largest potential for recovery since it has the largest strain of around 0.425. These two factors combine to allow for the large average local recovery of 0.294 across the three cycles to occur in the first strain localization region at this strain level. Comparatively lower recovery (0.161) occurs for the full sample since the macroscale strain is localized to only three regions thus decreasing the maximum observed (0.234) and resulting available recovery.

In contrast at ϵ_3 essentially all of the sample is experiencing larger amounts of localization (strain >0.40) as illustrated by Fig. 5a and e. A plateau occurs in the plot of the fraction of sample experiencing localization in Fig. 5a at above 0.95. This plateau is interpreted as the deformation accommodation methods that result in the formation of interfiber contacts being exhausted. Subsequently, the sample begins deforming more homogeneously and irreversible deformation avenues occur more readily. This is evident through the final strain localization region beginning to retain strains of between 0.008 and 0.036 after unloading as showcased in Fig. 5b and Table 3. With this occurring, it suggests that the model for the increase in interfiber contact density from Islam and Picu [34] is only valid up to a certain level of compaction. This then indicates that strengthening due to formation of interfiber contacts only occurs in the low ($\bar{\epsilon}_1$) to moderate strain ($\bar{\epsilon}_2$) regime, after which strengthening can most likely be attributed to collective deformation of the material and fiber bending/bowing. Fiber bending/bowing has been observed in SEM imaging at low to moderate strains [28] so it would follow that once all easier strengthening mechanisms have been exhausted, fiber bending/bowing would commence resulting in further strengthening.

4.2.2. Energy dissipation

The proposed shift in strengthening mechanism is also observed when investigating energy dissipation during the load-unload cycles. Evidence of energy dissipation is observed in the stress-strain curve of OOP Load-Unload as the hysteresis during the load-unload cycling. The individual values for energy loss coefficient can be seen in Table 4. For a similar carbon fiber network material, Zhang et al. calculated energy loss coefficients of less than 0.3 up to a strain of 40% with the coefficient increasing with increasing strain [28]. In this study, an increase in energy loss coefficient from 0.054 average to 0.337 average was observed between $\bar{\epsilon}_1$ and $\bar{\epsilon}_2$. The small increase in energy loss coefficient between $\bar{\epsilon}_2$ and $\bar{\epsilon}_3$ (0.359 average) does not meet the level of statistical significance. In the

Table 4
Energy loss coefficients.

Strain Level	Cycle 1	Cycle 2	Cycle 3
$\bar{\epsilon}_1 = 0.02$	0.016	0.061	0.084
$\bar{\epsilon}_2 = 0.23$	0.339	0.332	0.341
$\bar{\epsilon}_3 = 0.42$	0.349	0.371	0.358

work by Zhang et al. energy dissipation was attributed to fiber sliding [28]. This is still an available energy dissipation method for the material in this study, but more specifically it seems that energy dissipation is tied to the fraction of the material experiencing strain localization. With this being the case, it would follow that the majority of the energy dissipation is related to the engagement and disengagement of interfiber contacts, both of which create friction thus dissipating energy. Since the Islam and Picu model [34] for increase in interfiber contact density seems to apply well up to a strain of approximately 0.25, the increase in energy loss coefficient can be attributed to the large increase in interfiber contacts. After this point, however, there is minimal increase in interfiber contact density and thus a minimal increase in energy dissipation due to friction resulting in the similar energy loss coefficients at strains of 0.23 and 0.42. The bowing/bending of fibers for strengthening at higher strains does not create friction in the material and thus would not increase the energy loss coefficient. Looking at the energy loss coefficient values listed in Table 4, the values for $\bar{\epsilon}_2$ and $\bar{\epsilon}_3$ are above the 0.3 mark obtained by Zhang et al. [28]. In this work, though, irreversible deformation in the form of fiber/junction failure was shown to occur which also acts as an avenue for energy dissipation. The relative contributions of reversible dissipation compared to irreversible dissipation are not able to be determined from the present study. However, it is believed that the contribution of reversible dissipation is much larger given the increase in retained strain between $\bar{\epsilon}_2$ and $\bar{\epsilon}_3$ (0.157 average or 37.3% of the average maximum compressive strain at $\bar{\epsilon}_3$) is relatively larger than the increase in energy loss coefficient (0.022 or 6.1% of the average energy loss coefficient at $\bar{\epsilon}_3$).

5. Conclusions

In this study the correlation between the mesoscale localized deformation behavior and the resulting macroscale mechanical properties of fibrous, porous carbon materials was investigated. To this end, compression tests with corresponding DIC were completed on a porous carbon fiber network material. At the macroscale, the stress-strain behavior and corresponding mechanical properties were determined. At the mesoscale, information regarding the initiation, propagation, and growth of strain localization regions was obtained. These results were then tied together to improve the clarity of the relationship between the mesoscale and macroscale for fibrous, porous carbon materials. Important findings are summarized below.

- Deformation in the OOP direction initially occurs solely via reversible mechanisms (fiber sliding and movement) but shifts to a combination of reversible and irreversible mechanisms (fiber/junction failure) after yield.
- Increases in the formation of new interfiber contacts occurs up to a strain of approximately 0.30, after which the availability of new interfiber contacts has been exhausted.
- Strengthening during OOP loading is initially due to increases in interfiber contacts (and thus relative density) but transitions to collective material deformation and bowing/bending of fibers at strains of approximately 0.30 and higher corresponding with a plateau in the fraction of the material experiencing strain localization.
- Upon deformation in the IP direction, stress is directly applied to the fibers and junctions limiting the ability for reversible deformation mechanisms to operate and significantly changing the mechanical response compared to OOP loading.

Data availability

The raw/processed data required to reproduce these findings will be made available upon request.

CRedit authorship contribution statement

R.N. Quammen: Writing – review & editing, Writing – original draft, Visualization, Methodology, Investigation, Formal analysis, Data curation. **P.F. Rottmann:** Writing – review & editing, Writing – original draft, Visualization, Supervision, Resources, Project administration, Methodology, Investigation, Funding acquisition, Formal analysis, Conceptualization.

Declaration of competing interest

The authors declare that they have no known competing financial interests or personal relationships that could have appeared to influence the work reported in this paper.

Acknowledgments

This work was supported by NASA Kentucky Space Grant Consortium under NASA award 80NSSC20M0047. The authors would also like to acknowledge fruitful conversations with Catalin Picu, Matthew J. Beck, and Mujan N. Seif.

Appendix A. Supplementary data

Supplementary data to this article can be found online at <https://doi.org/10.1016/j.heliyon.2024.e27990>.

References

- [1] L. Liao, et al., A nanoporous molybdenum carbide nanowire as an electrocatalyst for hydrogen evolution reaction, *Energy Environ. Sci.* 7 (1) (2014) 387–392, <https://doi.org/10.1039/c3ee42441c>.
- [2] X. Liu, et al., High thermal conductivity and high energy density compatible latent heat thermal energy storage enabled by porous AlN ceramics composites, *Int. J. Heat Mass Tran.* 175 (2021/08/01/2021) 121405, <https://doi.org/10.1016/j.ijheatmasstransfer.2021.121405>.
- [3] Y. Zhu, P. Xu, X. Zhang, D. Wu, Emerging porous organic polymers for biomedical applications, *Chem. Soc. Rev.* 51 (4) (2022) 1377–1414, <https://doi.org/10.1039/d1cs00871d>.
- [4] H. Jee, K. Jeon, M.-J. Park, J. Lee, Fabrication of large area, ordered nanoporous structures on various substrates for potential electro-optic applications, *Appl. Sci.* 11 (24) (2021) 12136, <https://doi.org/10.3390/app112412136>.
- [5] Y. Huang, Y. Kong, L. Yan, H. Zou, Y. Chen, M. Liang, In situ construction of fiber-supported micro-porous char structure to enhance anti-ablative performance of silicone rubber composites, *Polym. Adv. Technol.* 32 (8) (2021) 2899–2907, <https://doi.org/10.1002/pat.5301>.
- [6] C. Richert, N. Huber, A review of experimentally informed micromechanical modeling of nanoporous metals: from structural descriptors to predictive structure–property relationships, *Materials* 13 (15) (2020) 3307, <https://doi.org/10.3390/ma13153307>.
- [7] J. Wang, C. Zhang, Y. Deng, P. Zhang, A review of research on the effect of temperature on the properties of polyurethane foams, *Polymers* 14 (21) (2022) 4586, <https://doi.org/10.3390/polym14214586>.
- [8] C.R. Picu, Constitutive models for random fiber network materials: a review of current status and challenges, *Mech. Res. Commun.* 114 (2021/06/01/2021) 103605, <https://doi.org/10.1016/j.mechrescom.2020.103605>.
- [9] Q. Liu, Z. Lu, Z. Hu, J. Li, Finite element analysis on tensile behaviour of 3D random fibrous materials: model description and meso-level approach, *Mater. Sci. Eng., A* 587 (2013/12/10/2013) 36–45, <https://doi.org/10.1016/j.msea.2013.07.087>.
- [10] L. Shi, et al., Compressive and shear performance of three-dimensional rigid stochastic fibrous networks: experiment, finite element simulation, and factor analysis, *J. Eur. Ceram. Soc.* 40 (1) (2020/01/01/2020) 115–126, <https://doi.org/10.1016/j.jeurceramsoc.2019.09.016>.
- [11] C.R. Picu, V. Negi, Compression of fibrous assemblies: revisiting the stress–density relation, *J. Appl. Mech.* 90 (2) (2022), [10.1115/1.4056180](https://doi.org/10.1115/1.4056180).
- [12] C.M. van Wyk, 20—note on the compressibility of wool, *J. Textil. Trans.* 37 (12) (1946/12/01 1946) T285–T292, <https://doi.org/10.1080/19447024608659279>.
- [13] S. Toll, J.-A.E. Manson, Elastic compression of a fiber network, *J. Appl. Mech.* 62 (1) (1995) 223–226, <https://doi.org/10.1115/1.2895906>.
- [14] F. Hild, S. Roux, Digital image correlation: from displacement measurement to identification of elastic properties - a review, *Strain* 42 (2) (2006) 69–80, <https://doi.org/10.1111/j.1475-1305.2006.00258.x>.
- [15] B. Pan, K. Qian, H. Xie, A. Asundi, Two-dimensional digital image correlation for in-plane displacement and strain measurement: a review, *Meas. Sci. Technol.* 20 (6) (2009) 062001, <https://doi.org/10.1088/0957-0233/20/6/062001>.
- [16] A. Abdulqader, D.C. Rizos, Advantages of using digital image correlation techniques in uniaxial compression tests, *Results Eng. in Engineering* 6 (2020/06/01/2020) 100109, <https://doi.org/10.1016/j.rineng.2020.100109>.
- [17] S. Sun, X. Chen, N. Badwe, K. Sieradzki, Potential-dependent dynamic fracture of nanoporous gold, *Nat. Mater.* 14 (9) (2015) 894–898, <https://doi.org/10.1038/nmat4335>.
- [18] C.E. Slone, J. Miao, E.P. George, M.J. Mills, Achieving ultra-high strength and ductility in equiatomic CrCoNi with partially recrystallized microstructures, *Acta Mater.* 165 (2019/02/15/2019) 496–507, <https://doi.org/10.1016/j.actamat.2018.12.015>.
- [19] Y. Xiong, N. Grilli, P.S. Karamched, B.-S. Li, E. Tarleton, A.J. Wilkinson, Cold dwell behaviour of Ti6Al alloy: understanding load shedding using digital image correlation and dislocation based crystal plasticity simulations, *J. Mater. Sci. Technol.* 128 (2022/11/20/2022) 254–272, <https://doi.org/10.1016/j.jmst.2022.05.034>.
- [20] M.R. Islam, G. Tudryn, R. Bucinell, L. Schadler, R.C. Picu, Morphology and mechanics of fungal mycelium, *Sci. Rep.* 7 (1) (2017/10/12 2017) 13070, <https://doi.org/10.1038/s41598-017-13295-2>.
- [21] K.E. Parmenter, K. Shuman, F. Milstein, C.E. Szalai, H.K. Tran, D.J. Rasky, Compressive response of lightweight ceramic ablators: phenolic impregnated carbon ablator, *J. Spacecraft Rockets* 38 (2) (2001) 231–236, <https://doi.org/10.2514/2.3675>.
- [22] Y. Zhang, et al., Compression behaviors of carbon-bonded carbon fiber composites: experimental and numerical investigations, *Carbon* 116 (2017/05/01/2017) 398–408, <https://doi.org/10.1016/j.carbon.2017.02.012>.
- [23] Y. Chen, et al., Fabrication and ultra-high-temperature properties of lightweight carbon-bonded carbon fiber composites, *Ceram. Int.* 45 (17) (2019/12/01/2019) 22249–22252, <https://doi.org/10.1016/j.ceramint.2019.07.250>. Part A.
- [24] R. Fu, S. McDaniel, M. Beck, A. Martin, Crack modeling in charring ablation materials, in: *AIAA Scitech 2021 Forum, AIAA SciTech Forum: American Institute of Aeronautics and Astronautics*, 2021.
- [25] W. Schill, L.J. Abbott, J.B. Haskins, A multiscale cohesive law for carbon fiber networks, *Carbon* 171 (2021) 376–384, <https://doi.org/10.1016/j.carbon.2020.09.007>.
- [26] G. Luo, et al., Compressive damage of three-dimensional random fibrous ceramic materials: a meso-mechanics modeling and experimental study, *Ceram. Int.* 44 (13) (2018/09/01/2018) 15690–15699, <https://doi.org/10.1016/j.ceramint.2018.05.241>.
- [27] P. Agrawal, J.F. Chavez-Garcia, J. Pham, Fracture in phenolic impregnated carbon ablator, *J. Spacecraft Rockets* 50 (4) (2013) 735–741, <https://doi.org/10.2514/1.a32389>.
- [28] Y. Zhang, et al., Resilient carbon fiber network materials under cyclic compression, *Carbon* 155 (2019/12/01/2019) 344–352, <https://doi.org/10.1016/j.carbon.2019.08.070>.
- [29] M. Sutton, J.-J. Orteu, H. Schreier, *Image correlation for shape, motion and deformation measurements. Theory and Applications, Basic Concepts*, 2009.
- [30] M. Simonsen, "Strain Tensors and Criteria in Vic." *Correlated Solutions*. <https://correlated.kayako.com/article/2-strain-tensors-and-criteria-in-vic> (accessed June, 2022).
- [31] J.A. Sharon, K. Hattar, B.L. Boyce, L.N. Brewer, Compressive properties of (110) Cu micro-pillars after high-dose self-ion irradiation, *Mater. Res. Lett.* 2 (2) (2014) 57–62, <https://doi.org/10.1080/21663831.2013.859179>.
- [32] P.J. Noell, J.D. Carroll, B.L. Boyce, The mechanisms of ductile rupture, *Acta Mater.* 161 (2018/12/01/2018) 83–98, <https://doi.org/10.1016/j.actamat.2018.09.006>.
- [33] L. Mezeix, C. Bouvet, J. Huez, D. Poquillon, Mechanical behavior of entangled fibers and entangled cross-linked fibers during compression, *J. Mater. Sci.* 44 (14) (2009/07/01 2009) 3652–3661, <https://doi.org/10.1007/s10853-009-3483-y>.
- [34] M.R. Islam, R.C. Picu, Effect of network architecture on the mechanical behavior of random fiber networks, *J. Appl. Mech.* 85 (8) (2018), <https://doi.org/10.1115/1.4040245>.
- [35] S. Toll, Packing mechanics of fiber reinforcements, *Polym. Eng. Sci.* 38 (8) (1998) 1337–1350, <https://doi.org/10.1002/pen.10304>.
- [36] D. Poquillon, B. Viguiere, E. Andrieu, Experimental data about mechanical behaviour during compression tests for various matted fibres, *J. Mater. Sci.* 40 (22) (2005/11/01 2005) 5963–5970, <https://doi.org/10.1007/s10853-005-5070-1>.